

SCIENTIFIC REPORTS

OPEN

Designing of metallic nanocrystals embedded in non-stoichiometric perovskite nanomaterial and its surface-electronic characteristics

Jagadeesh Suriyaprakash^{1,2}, Y. B. Xu¹, Y. L. Zhu¹, L. X. Yang¹, Y. L. Tang¹, Y. J. Wang¹, S. Li^{1,2} & X. L. Ma^{1,3}

Engineering of novel functional nanocomposite as like as the metallic nanocrystals supported non-stoichiometric perovskite nanomaterial in controlled parameters (size, shape and ratio of chemical characteristics) is a challengeable task. In this context, we present a facile route to fabricate and study its physicochemical property at real time mode in this report. Nanoscale pure Pb crystals surfaced on non-stoichiometric A-site deficient $\text{Pb}_{1-x}\text{TiO}_{3-y}$ nanoparticle were fabricated when a precursor lead titanate (PbTiO_3) nanoparticle was exposed to an electron beam irradiation (EBI) in a transmission electron microscope (TEM) at ambient temperature. In the state of the art, the chemical states and electronic structure of non-irradiated and irradiated PbTiO_3 were studied by X-ray photoelectron spectroscopy (XPS). Electron bombardment resulted in a new visible feature at low binding energy in the Pb 4f core level, while Ti 2p and O 1s line shape showed slight changes. The Fermi level of the corresponding materials was determined to be 1.65 ± 0.1 eV and 2.05 ± 0.1 eV above the valence band maximum, respectively. The normal, weakly p-type PTO exhibits peculiar n-type feature after EBI process (The Fermi level moves near to the conduction band). A feasible mechanism is proposed involving the electron-stimulated local bond-breaking phenomenon in PbTiO_3 .

Perovskite type ABO_3 materials are of immense interest due to their potential application, especially titanates ATiO_3 (Where A = Ba, Sr, Ca, Pb) family exhibits extraordinary optical, electrical and magnetic properties in both bulk and nanoscale region¹⁻⁶. Considerable research has been focused on the fabrication of these multifunctional materials from the last three decades achieved by modification of the materials (structure, shape, composition, defects and etc)⁷⁻¹⁰. Growing interest has been propelled in the probe of non-stoichiometric transition metal titanates ($x\text{A-A}_{1-x}\text{TiO}_{3-y}$) materials. Defected and impurities implanted (doping) perovskites have been studied intensively. $\text{A}_{1-x}\text{B}_x\text{TiO}_{3-y}$ (Where A and B are transition or alkali metals; $\text{A} \neq \text{B}$) type materials are synthesised by physical as well as chemical methods in earlier studies¹¹⁻²⁶. Despite the fact that perovskite nanomaterials have been extensively investigated over the past decade, to the best of our knowledge, the fabrication of A-site void $x\text{A-A}_{1-x}\text{TiO}_{3-y}$ type nanocomposite by electron beam irradiation, surface characteristics and its formation mechanism has not been described thus far. The new nanoscale structures interacting with electron beam has been primarily studied by transmission electron microscopy (TEM). *In situ* observation study of electron and matter interaction has been carried out in metals (Au, Pt, In, Ag, Mo, Bi, Ni and Li)²⁷⁻³², metal oxides (Li_2O , WO_3 , V_2O_5 , Fe_3O_4)³³⁻³⁵, semiconductors (Si, Ge, GaP, GaAs, CdS, InN, ZnS)³⁶⁻⁴⁰, carbon nanotube (CNT)^{41, 42} and ceramics (Pb-PST , BaTiO_3 , LaPO_4 , ScPO_4)⁴³⁻⁴⁷. The main purpose of this work is to address the question of the role of electron beam irradiation on the ABO_3 nanomaterial and its electronic structure modification. In addition, to reveal the formation mechanism of the novel metal supported non-stoichiometric $x\text{A-A}_{1-x}\text{TiO}_{3-y}$ type nanomaterials is also important. We chose PbTiO_3 (PTO) as a prototypical material because its lattice parameters, phase transition, bonding nature and mass value are simple. Besides, PTO is a classic example of ferroelectric perovskite with high

¹Shenyang National Laboratory for Materials Science, Institute of Metal Research, Chinese Academy of Sciences, 72 Wenhua Road, 110016, Shenyang, China. ²University of Chinese Academy of Sciences, 100039, Beijing, China. ³State Key Laboratory of Advanced Processing and Recycling of Non-ferrous Metals, Lanzhou University of Technology, 730050, Lanzhou, China. Correspondence and requests for materials should be addressed to X.L.M. (email: xlma@imr.ac.cn)

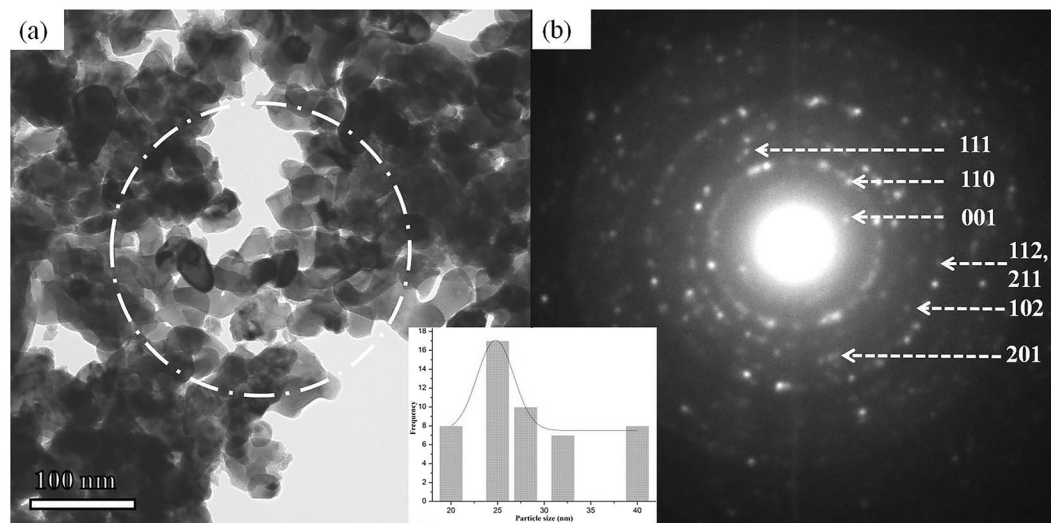


Figure 1. (a) Low magnification TEM image of as-prepared PTO sample, (b) Corresponding SAED pattern of circled area. The inset is a size distribution curve of the particles.

tetragonality and it exhibits a unique negative thermal expansion in the perovskite family, which has been widely used both in academic research and device application. The large ionic shift leads to a large spontaneous polarization, which is in fact among the largest in the perovskite family. Moreover, a double layer perovskite system, $\text{Bi}_4\text{Ti}_3\text{O}_{12}$ (BiTO) also utilized for sake of the reliability of this innovative technique.

In this article, we report a simple method to fabricate the pure Pb nanoparticles supported on non-stoichiometric PbTiO_3 nanomaterial by electron beam irradiation. The growth mechanism of the metal nanoparticles and its structural stability were investigated. An x-ray photoelectron spectroscopy study revealed the surface characteristic as well as electronic structure of the non-irradiated and irradiated PTO nanomaterials. This study disclosed that the electron irradiation can be utilized as one step route to fabricate the novel $x\text{A}-\text{A}_{1-x}\text{TiO}_{3-y}$ perovskite nanocomposite and to get the knowledge of dynamic behaviour of an unstable nanoscale perovskite material in TEM, which leads to understanding of the dynamics of phase transformations and the atomistic nature of bonding. In addition, we observed the same phenomenon in the BiTO material (See Supplementary Information).

Results

Morphology and crystal structure of PbTiO_3 and $x\text{Pb}-\text{Pb}_{1-x}\text{TiO}_{3-y}$ nanostructures. To provide more insight into the structural and the morphology of the synthesised material, we carried out XRD as well as TEM studies before the irradiation process. Figure 1(a) shows the TEM images of the as-synthesised sample. The shapes of the most particles are spherical with the particle size of 18–40 nm. Few particles are found to be clustered in a chain due to agglomeration of the particles. The selected area electron diffraction pattern (SAED) taken over a large area indicative in a white circle in Fig. 1(a) illustrated that polycrystalline PbTiO_3 is present. The SAED pattern of Fig. 1(b) reveals diffraction rings indicative of the random crystallographic orientations of the nanocrystal of the synthesised material. All diffraction rings are indexed as those of a tetragonal structure of PTO consistent with the XRD data (See Supplementary Information Fig. S1).

We found that the pure Pb nanoparticles supported on NPTO (here after NPTO refers non-stoichiometric PbTiO_3) nanoparticle could be synthesised by electron beam irradiation of PbTiO_3 nanoparticle. Intriguingly, The Pb metal nanoparticle and non-stoichiometric PbTiO_3 (Pb-NPTO) nanomaterial coexisted. In this Pb-NPTO nanostructure, The Pb nanocrystals were observed to form and grow within the PTO matrix by electron bombardment, which enhances the growth of nanocrystals. As shown in Fig. 2 and Fig. S2 in the Supplementary Information, the PTO nanoparticles were exposed under electron beam with current density ($J = 2.02 \times 10^7 \text{ A/m}^2$). The size of Pb nanoparticles ranges from 4 nm to 15 nm which are observed throughout this study. We examined various PTO nanoparticles exposed under EBI to investigate the structural change and evolution of Pb nanocrystals.

In Fig. 2, HRTEM image evidently illustrates about Pb-NPTO structure. Fast Fourier transform (FFT) patterns of two different selected areas are shown in Fig. 2, namely 1 and 2. The bright spots in the pattern 1 can be well indexed to the $(1\bar{1}1)$, (002) and $(\bar{1}11)$ planes of cubic Pb, which belongs to the $Fm\bar{3}m$ (No. 225) space group and the bright spots in the pattern 2 can be well indexed to the (001) plane of tetragonal PTO. The lattice fringe spacing suggests that this particle is the tetragonal PTO, which belongs to the $P4mm$ (No. 99) space group and has a lattice parameter of $c = 4.156 \text{ \AA}$ and $a = 3.905 \text{ \AA}$. The outcome of *in situ* HRTEM study furnishes the formation, growth and coagulation of Pb nanocrystals. The nucleation and growth of a nanoparticle are shown as a function of time in the series of images presented in Fig. S3 (See Supplementary Information). It shows the existence of a 4–8 nm breadth of Pb nanoparticles at the circumference of the NPTO nanoparticle.

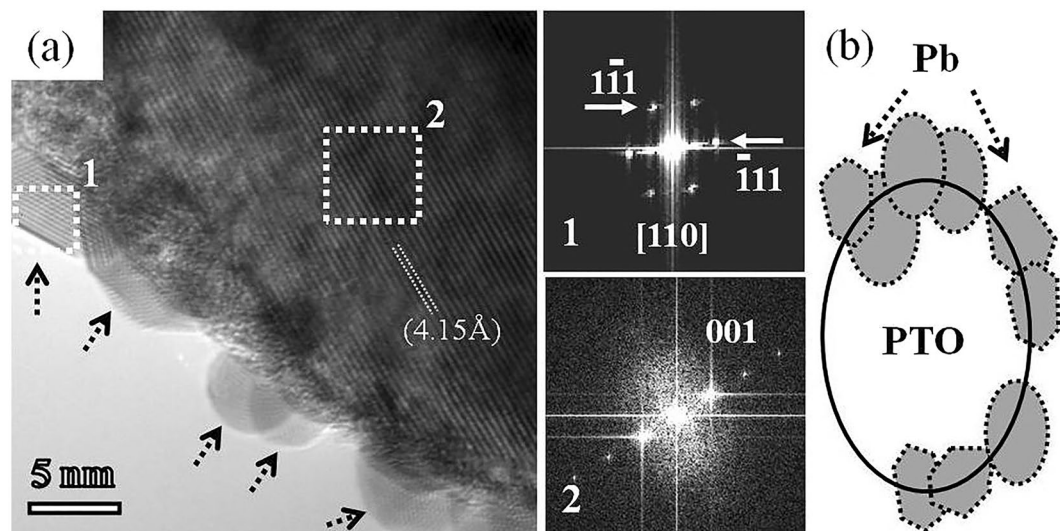


Figure 2. (a) HRTEM image of Pb-NPTO nanomaterial. The right side image 1 and 2 are corresponding FFT pattern of Pb and PTO, respectively (Where the selected area shown in (a) by white dotted rectangles). (b) A model diagram portrays the Pb-PTO coexisting structure.

Initially, no Pb nanoclusters/crystals are observed on the PTO nanoparticle with the size of 30 nm. Increasing the EBI time to a critical value of 20 sec (with a 300 KeV electron beam, $J = 2.02 \times 10^7 \text{ A/m}^2$) resulted in the formation of many sphere like particles appearing on the PTO nanoparticle (indicated by the arrow). The number and the size of newly formed Pb nanoparticle increase with increasing the irradiation time. This newly formed nanoparticle is about 4 nm wide. After 40 sec, the width of the nanoparticle is increased to 7 nm which is about twice the width of the individual Pb nanoparticle. Prolonged irradiations on the sample affect the nature of the material. To elucidate the possible electron beam effect on the structure, we have recorded *in situ* TEM image of two different PTO nanoparticles under long periods of EBI (Movie S1 and Movie S2 in the Supplementary Information).

An extensive experimental result shows that pure Pb nanoparticles have different morphologies such as single crystal, twinned and multiple twinned. It is found that the Pb nanocrystals show structural fluctuation under intense electron-beam irradiation as other metal nanocrystals like gold, Indium, platinum, palladium and etc.^{27,28,43}. A single crystal of lead (Pb) in the size of 4 nm is observed in Fig. 3(a) along with PTO nanoparticle, which is exposed in EBI. The fast Fourier transformation (FFT) processing patterns of two areas in Fig. 3(a), shown as 1 and 2 on the right side of the Fig. 3(a), belong to PTO and Pb crystals, respectively. It is found that the bright spots in the pattern 1 can be well indexed to the (001), ($\bar{1}10$) and ($\bar{1}11$) planes of tetragonal PTO and also the pattern 2 can be well indexed to the ($1\bar{1}1$), ($\bar{1}11$) and (002) planes of cubic Pb viewed along [110] zone axis. The calculated spacing of the lattice fringes of the nanoparticle in Fig. 3(b) is about 4.1 Å and 2.7 Å, which is corresponding to the PTO crystal planes (100) and (110), respectively. Moreover, the spacing of the lattice fringes of the nanoparticle $d_{(111)} = 2.8 \text{ Å}$ in Fig. 3(c) belongs to the pure Pb in face-centered-cubic (fcc) structure with a lattice constant 4.9 Å. These results validated that the nanoparticles are a mixture of both pure Pb and PbTiO_3 coexisting in the same environment. Note that, oxide or other impurities were not observed on the surface of the nanoparticle. To confirm this we looked for other oxides i.e. PbO_2 , Pb_2O_3 , TiO_2 , etc. However, these oxides were not presented in this system. To elucidate the TEM image of the Fig. 3(b) and (c), we compared the simulated HRTEM image and the obtained one from experiment. Figure S4 in the supplementary Information shows the simulated HRTEM images, which is consist with the PTO and Pb material.

Twinned structures are regularly observed in the fcc structured metal nanoparticles^{48–51}. Twin boundaries (TBs) are coherent planar defects where atom arrangements on one side are mirror reflections of those on the other side. In fcc metals, low energy twin planes are of {111} type that enclose an angle of 70.53° . Figure 4(a) shows a HRTEM image of the twinned Pb nanoparticles on the PTO matrix. The right side images are the corresponding FFT pattern of the selected areas, namely 1, 2 and 3 in the Fig. 4(a). The 1 and 3 selected area in the Fig. 4(a) are on the twin structures, 2 is off the twin structure. The FFT pattern of 1 and 3 is similar and the bright spot can be indexed as the ($1\bar{1}1$), ($\bar{1}11$) and (002) planes of cubic Pb viewed along [110] zone axis. The spots from twin structure are vividly observed in the FFT pattern and depicted by rectangles. Figure 4(b) is the Fourier filtered image, clearly shown the twin boundaries. The twin boundaries are denoted by black arrow in Fig. 4(a,b). There are two twin boundaries observed in the single Pb nanoparticles, which appeared as zigzag shape. In addition, we observed the multiple twinned Pb structure, which is illustrated in Fig. S5 (See Supplementary Information).

To make sure that Pb-NPTO nanocomposites are produced by exposure to the electron beam and not by rapid localized specimen heating followed by specimen melting process, the electron beam first focused on to arbitrary area and after that shifted and focused on various PTO nanoparticles that were not previously exposed to the e-beam. As shown in obtained images are various Pb-NPTO nanocomposite structures obtained from different

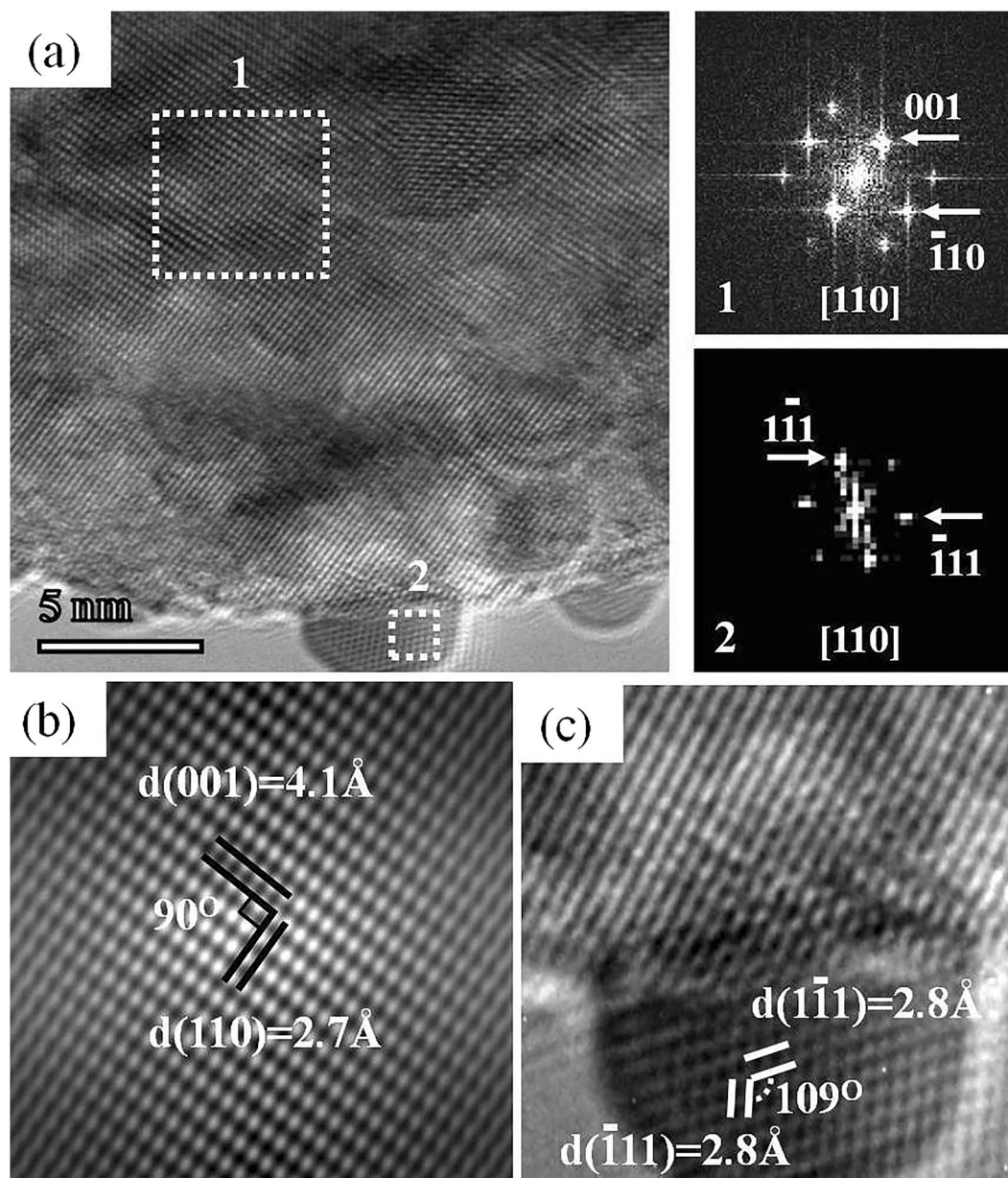


Figure 3. (a) TEM image of Pb-PTO nanomaterial. The right side image 1 and 2 are corresponding FFT patterns of PTO and Pb respectively, the selected area shown in Fig (a) by dotted rectangles. (b) FFT filtered image of the selected area as denoted 1 in Fig (a). (c) FFT filtered image of the selected area around Pb nanocrystal.

precursor. In the process, The Pb nanoparticle population increased with EBI time, we discovered that the population as well as the size of Pb nanoparticles remains constant, when the irradiation is suspended. To affirm that we took a few unfocused TEM images, which are not greatly exposed to the EBI (Fig. S6 in the Supplementary Information). While in deliberate Pb nanocrystal structural study, the e-beam was highly focused on the particular Pb nanocrystal and it exhibits structural fluctuation other than nearby Pb nanocrystals. It demonstrates that pure metallic characteristic Pb nanocrystal is coexisted with NPTO nanoparticle. To the best of our knowledge, this novel nanocomposite has seldom been observed in perovskite material under EBI in real time observation.

X-Ray Energy Dispersive Spectroscopy (EDS) analysis. In order to study the changes in chemical composition of the material, we exploited EDS method at different stages during the irradiation process. Figure 5 shows the typical EDS spectrum at different stages of irradiation. The spectrum acquired at the beginning of the experiments shows Pb, Ti and O peaks (inclusive of Cu and C peaks which belong to the sample grid). At this point, the semi-quantitative analysis was consistent with the atomic composition with the PbTiO_3 . After sample irradiated under e-beam, the EDS spectrum of the sample shows that the oxygen to Pb/Ti ratio decreased significantly, which argues that the particles consist of non-stoichiometric PbTiO_3 . Prolonged irradiation decomposed

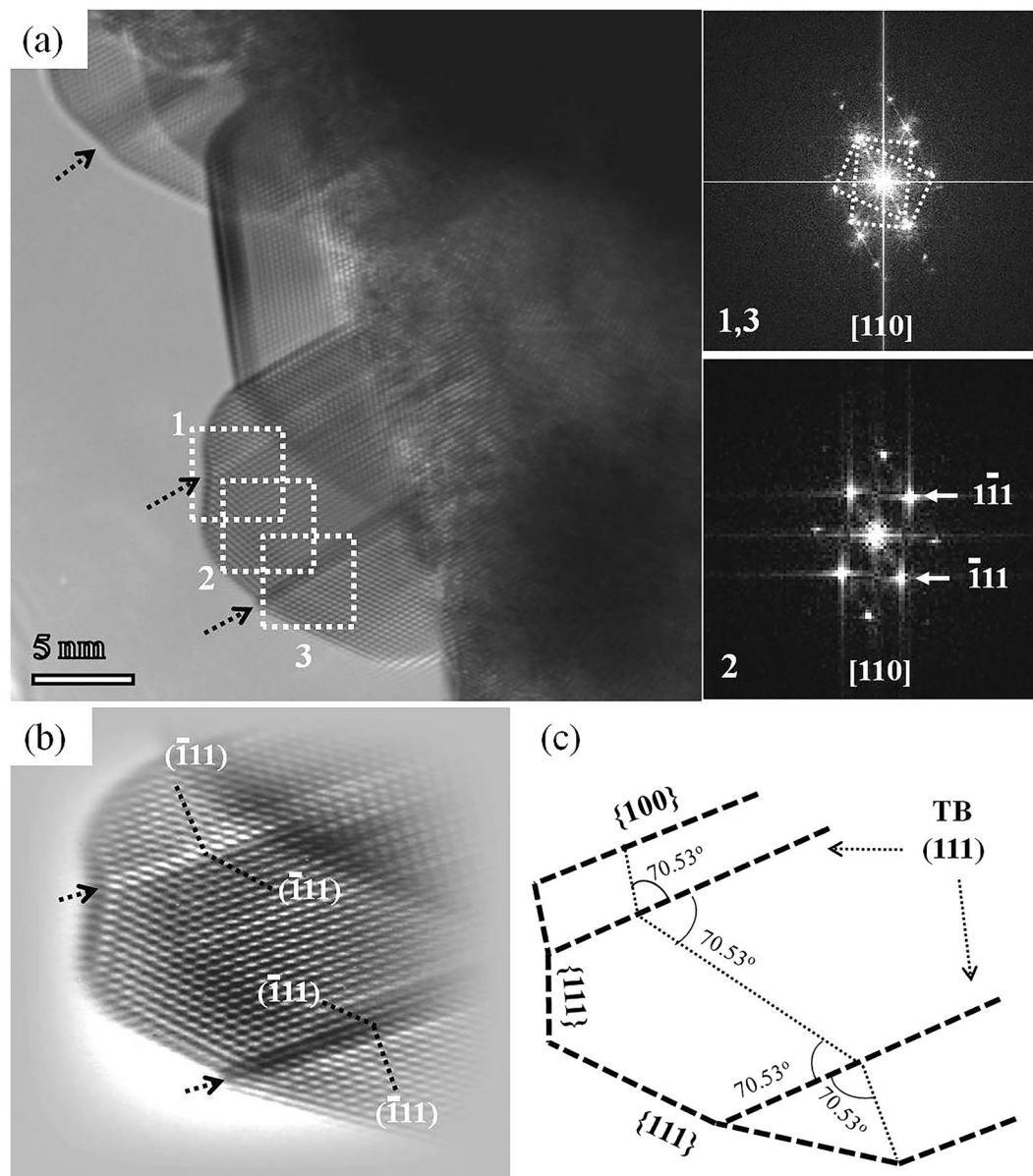


Figure 4. (a) HRTEM image of twinned Pb-PTO nanomaterial in $[110]$ zone axis. The right side images 1, 3 and 2 are corresponding FFT pattern of twinned Pb, the selected area shown in Fig. 4 (a) by dotted rectangles. (b) FFT image of the twinned Pb nanocrystal in Fig (a). (c) Schematic diagram of the twinned Pb nanocrystal.

a PTO nanoparticle entirely. Consequently Pb nanoballs are formed around the amorphous matrix, which can be viewed in the EDS spectrum.

Figure S7 in the Supplementary Information illustrates TEM and HAADF-EDS spectrum elemental mapping images of the PTO nanoparticle before and after irradiation in identical region. The obtained data for different Pb, Ti and O concentrations revealed an excess of Pb with a deficiency in oxygen. The deficiency in O due to electron-stimulated desorption process (ESD) followed by oxygen lost in the vacuum. These results supported that the volatilization of Pb does take place in this process, as an alternative it forms a novel Pb supported $Pb_{1-x}TiO_{3-y}$ system. At the initial point, the clear PTO nanoparticle were seen in the TEM image, after irradiated by electron beam the material morphology was turned into fuzzy cloud appearance due to the arrangement of small Pb nanoballs on the surface of the sample. To derive the exact chemical formula, we calculated the atomic percent (at. %) value from elemental mapping spectrum at the different area of scanned region. The values and scanned region are bestowed in detail in the Supplementary Information.

X-Ray Photoelectron Spectroscopy (XPS) analysis. Surface features and electronic band structures of non-irradiated and irradiated PTO nanomaterials were examined using XPS and Gaussian fitting. The XPS survey spectra of the two samples are shown in Fig. S10 (Supplementary Information). As expected, the spectrum of the non-irradiated PTO shows higher Pb than observed in the irradiated PTO. It can be seen that the materials

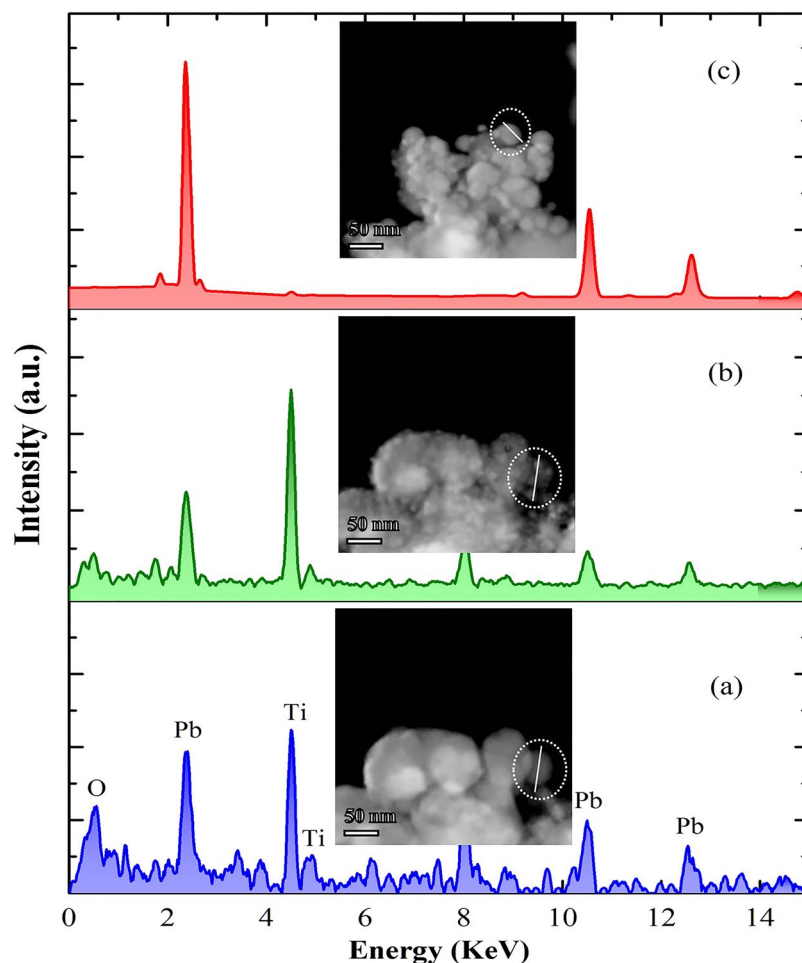


Figure 5. (a,b and c) are EDS spectrum acquired from the PbTiO_3 sample before, after 80 sec and prolonged point of irradiation, respectively. The insets are corresponding High angle annular dark field (HAADF) images of the sample, which are analyzed by EDS method. The circle denoted a line profile scanned region.

consists of Pb, Ti and O elements along with C 1s peak. Figure 6(a–c) shows narrow scan XPS spectra of Pb 4f, Ti 2p and O 1s, respectively, of a non-irradiated PTO sample. The Pb 4f spectra can be deconvoluted into two major and two minor components of Pb $4f_{7/2}$ and Pb $4f_{5/2}$ as observed in Fig. 6(a). The major peaks at 138 and 142.9 eV are attributed to lead lattice in PTO crystal. The minor peaks at 139.4 and 144.2 eV may arise due to the formation of negligible amount of air species⁵². The spin-orbit splitting ($\Delta(4f_{7/2}-4f_{5/2})$) for Pb 4f is 4.9 eV, which is consistent with the PTO nanowire value⁵³. Ti 2p deconvoluted spectrum shows only one spin orbit doublet as shown in Fig. 6(b). The first component around 459.2 eV is attributed to Ti $2p_{3/2}$ peak, whereas the second one around 464.8 eV is attributed to Ti $2p_{1/2}$ peak, which are larger than those reported for the PTO ceramics⁵⁴. The difference between Ti $2p_{3/2}$ and Ti $2p_{1/2}$ spin-orbit splitting is 5.6 eV, which is well matched with the earlier reported ferroelectric materials with Ti atom in TiO6 octahedron⁵⁵. The O 1s spectrum can be deconvoluted into three components as shown in Fig. 6(c). The major peak of higher binding energy 531.8 eV is assigned to adsorbed oxygen, the second major component at low binding energy 530.1 eV is assigned to lattice oxygen in the PTO. Figure 6(d–f) shows core-level XPS spectra of Pb 4f, Ti 2p and O 1s, respectively, of an irradiated PTO sample. Considering Pb 4f and O 1s spectra, the irradiated sample shows significant alterations in its surface characteristic with its counterpart non-irradiated PTO. It's clearly seen that Pb 4f doublet exhibits two Pb $4f_{7/2}$ components at 136.3 eV and 138 eV. The peak at 138 eV is attributed to Pb at perovskite lattice and its intensity is lower than the non-irradiated Pb 4f spectrum. The lower binding energy components at 136.3 eV is assigned to Pb metal. The calculated downward shift binding energy is 1.7 eV. This indicates that the Pb metal co-exists with the non-stoichiometric PTO. As we discussed earlier, the Pb metal formed by the reduction of Pb^{2+} ions to Pb^0 . T J Zhu *et al.*⁵⁵ reported the same phenomenon when the sample was sputtered by Ar^+ ion. Moreover, in Fig. 6(e) O 1s spectrum of irradiated sample shows two components at 530.5 and 532.1 eV. In contrast, we did not observe any significant difference between Ti 2p spectrum of non-irradiated and irradiated PTO samples as shown in Fig. 6(f).

As a consequence of electron bombardment new electronic states appear in the bulk band gap and the structure of the valence band is changed. Figure 7(a) shows valence band spectrum of the non-irradiated and irradiated PTO. For the non-irradiated PTO, the band A region consists basically of O 2p states hybridized with Pb 6s, Pb 6p and Ti 3d states, this region is the evidence for the Pb–O–Ti bonding interaction. The total width of the region is approximately 6 eV. The band B region is assigned to mainly Pb–O bonding interaction. A.T Kozakov

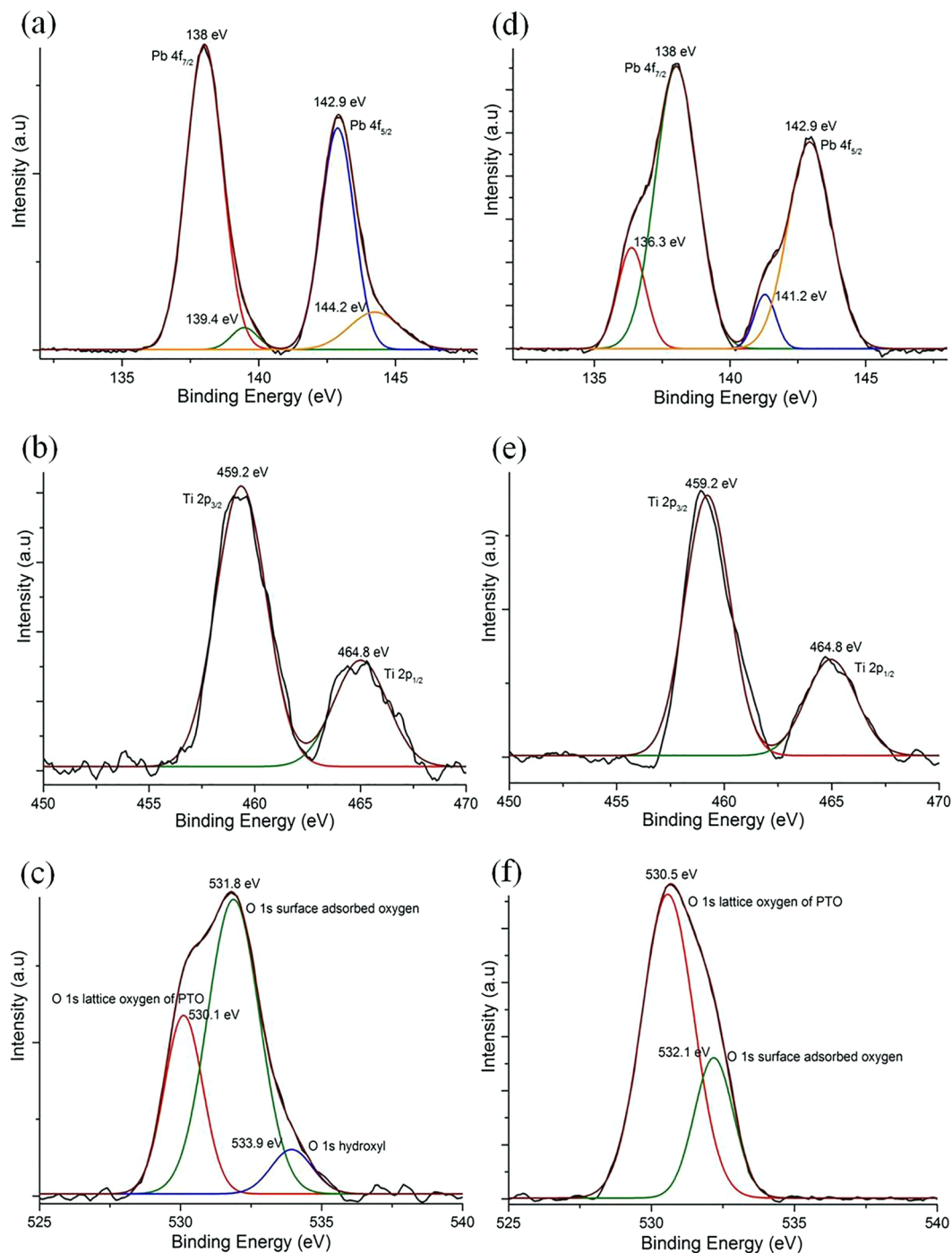


Figure 6. (a–c) XPS spectra of non-irradiated PTO nanoparticle. (d–f) XPS Spectra of irradiated PTO nanoparticle. From top to bottom core level spectra of Pb 4f, Ti 2p and O 1s plotted with deconvoluted spectra.

*et al.*⁵⁶ demonstrated that the B region was diminished when the Pb content becomes to zero in $\text{Pb}_{1-x}\text{Ba}_x\text{TiO}_3$ materials. The irradiated PTO valence band structure shows significant changes in the region of A and B band. The total width of A region is 5.7 eV. The intensity of the B region reduces due to the diminishment of the Pb–O bond interaction. As shown in Fig. 7, by taking the baseline intercept of a linear fit to the valence band edge, the valence band maximum (VBM) energy positions in the non-irradiated and irradiated PTO were determined to be 1.65 ± 0.1 eV and 2.05 ± 0.1 eV, respectively. The change in VBM position can be understood by the theory of metal–semiconductor contact. Before irradiation, the VBM of PTO nanoparticle is 1.65 ± 0.1 eV, which indicates that PTO nanoparticle is weak p-type (the band gap of PTO is 3.4 eV). After irradiation, the newly formed metallic Pb nanoparticles contact with PTO nanoparticle, changing the Fermi level and thus VBM⁵⁷. The Schottky limit of the valence band offset can be determined as 2.6 eV, from the work function of Pb (4.3 eV), and the electron affinity and band gap of PTO (3.5 and 3.4 eV). The Bardeen limit of valence band offset for PTO (1.95 eV) has

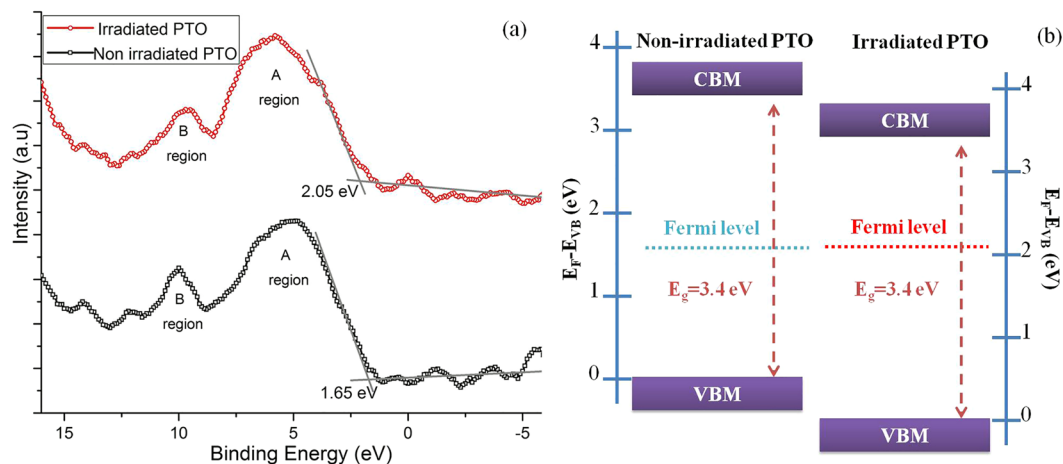


Figure 7. (a) valence band spectra of non-irradiated and irradiated PTO nanoparticle. (b) Band alignment structure of the non-irradiated PTO and irradiated PTO.

been calculated by Robertson, assuming the metal-induced gap states model. Our experimentally determined VBM of Pb/PTO located at 2.05 ± 0.1 eV below the Fermi level, which is between the two limits and more close to the Bardeen limit. The limits of Fermi level variation study of the $\text{PbTiO}_3/\text{SrTiO}_3$ interface reveals that the Fermi level increase with the increase of STO thickness on the PTO⁵⁸. The deposition of STO modified the Pb 6s electron contribution in the VBM of PTO. Surprisingly, we observed the same phenomenon in the Pb metal nanoparticle embedded in the $\text{Pb}_{1-x}\text{TiO}_{3-y}$ nanomaterial.

Discussion

Electron radiation damage of materials in the TEM study is commonly observed phenomenon⁵⁹. The lead titanate nanoparticle transforms into pure lead non-stoichiometric lead titanate (Pb-NPTO) nanocomposite system under electron irradiation. The bright field images and corresponding FFT pattern clearly show the low stability of the PTO and the induced reduction of Pb^{2+} ions by electron irradiation. The coexistence of pure Pb and NPTO is observed throughout this study. Though, there are many literatures discussed on the electron-materials interaction, each system has to deal with particular concern. The absolute mechanism of formation of the Pb-NPTO system by electron irradiation is still not understood. We provide the feasible mechanism of this phenomenon. When an electron interacts with the matter at high momentum, there are two possibilities of the mechanism involved i.e. elastic scattering and inelastic scattering. Both alter the nature of the materials by electrostatic charging, atomic displacement, specimen heating, mass loss and radiolysis process. We believe that electron beam sputtering or ionization of PbTiO_3 occurs in this study. To deduce the formation mechanism of the Pb-NPTO system, we resolve (a) atomic displacement and radiolysis, (b) specimen heating processes caused by incident electrons.

Atomic displacement and radiolysis: Atomic displacement will occur when the incident electron energy (E_0) exceeds the displacement energy of the materials (which is depending on the nature of the specimen-thickness, binding energy, cohesive energy and etc) at high angle elastic scattering. The energy transferred from the incident electron to the atomic nucleus is given by^{60–62}.

$$E = E_{max} \sin^2(\theta/2) \quad (1)$$

$$E_{max} = [2 E_0(E_0 + 2m_e c^2)]/M c^2 \quad (2)$$

Where θ is the deflected angle of the electron in the field of atom nucleus, E_0 and E_{max} are the incident electron energy and maximum energy in eV (which is transferred at $\theta = 180^\circ$) respectively, m_e and M are the mass of the electron and the nucleus in Kg, respectively, c is the speed of the light in m/s. The maximum energy transferred from the 300 KeV electron beam to Pb, Ti and O are 4.3 eV, 18.8 eV and 56.4 eV, respectively, which are calculated from the equation (2), such high energies are able to generate the atomic displacement and also mass transfer in the material. R F Egerton *et al.*⁶⁰ showed that the electron beam sputtering could occur by 200 KeV electrons for light and medium-Z atoms (including Au and Pb elements). Hence the sputtering process mainly involves low-Z atom oxygen in our case due to high E_{max} value. However, in insulating material like PbTiO_3 the knock-on displacement process is quenched due to the high density of the delocalized electron (while favourable in the conducting material). Withal, we observed the Pb and O atom displacement in this system. To shed more light on this growth mechanism, we considered the radiolysis process too (which occurred by electron beam degradation through inelastic scattering).

The incident electron beam breaks the bond between Pb-O rather than Ti-O, which is located on the surface of the PbTiO_3 structure and longer, since the required threshold energy of surface atomic displacement is lower than the interstitial site (Ti) atomic displacement. Here Pb^{2+} ions are reduced to Pb and the cation vacancy can be obtained in the crystal. Continuous irradiation affects the structure and leads to more bond breaking and

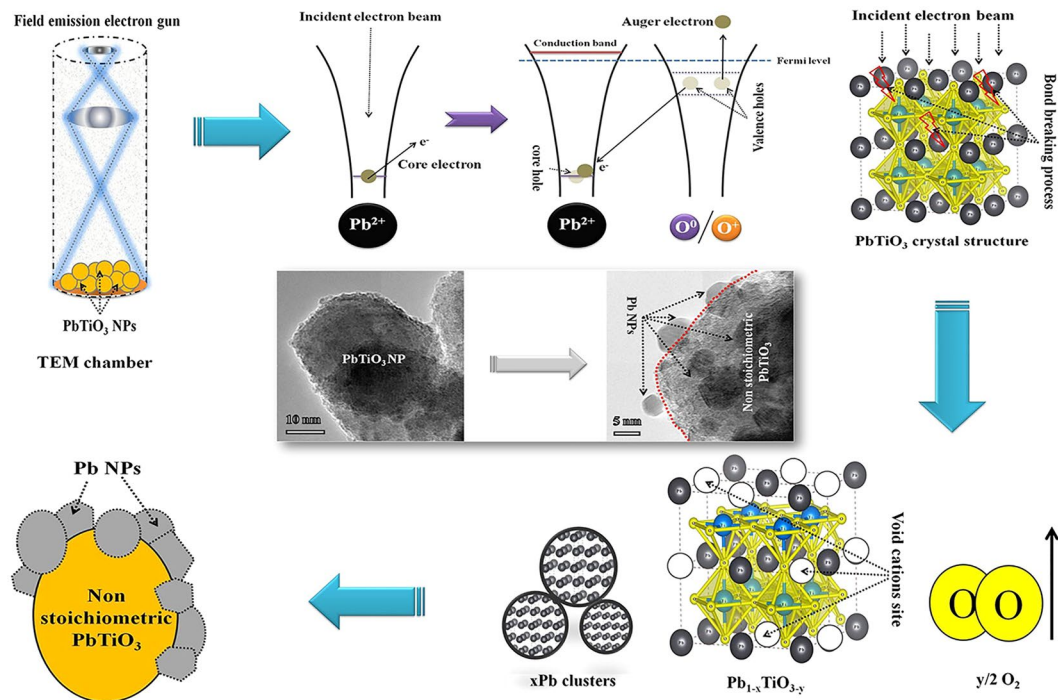
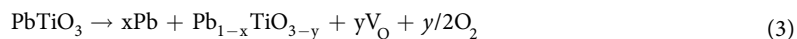


Figure 8. A schematic expression of formation of $x\text{Pb-Pb}_{1-x}\text{TiO}_{3-y}$ via Knotek-Feibelman (KF) mechanism.

produces the Pb on the surface of the degraded material. The number of Pb nanoparticles increases with the time of the radiation. Usually the cation vacancy occurs with an oxygen vacancy (Schottky defects) and tends to form the pair of cation and oxygen compounds like PbO , PbO_2 , Pb_2O_3 but we observed only pure Pb metal nanoparticle on the surface. And also, neither Ti-O bond breaking nor newly formed Ti_xO_y like compound were observed, indicating that desorption of the oxygen atom takes place and the oxygen lost into the vacuum. These results are highly consistent with the EDS and XPS analysis. Earlier studies have been proven that the electron-stimulated desorption occurs in transition-metal oxides (such as WO_3 , TiO_2 , LiNbO_3) via Knotek-Feibelman (KF) mechanism. Agreeing to the KF mechanism, the core hole/inner-shell vacancy created on the metal ion (Pb^{2+}) by the incident electron is followed by (interatomic) Auger decay from the oxygen³⁴. The mechanism expressed by following equation⁴⁶.



Where V_O is the oxygen vacancy, Our deliberate study of structural analysis of this system revealed that the pure Pb and non-stoichiometric PbTiO_3 coexisted as well as the Pb metal nanoparticles show structural fluctuation under electron irradiation as like other metal nanoparticles. In general notation the fabricated material via electron beam irradiation is $x\text{Pb-Pb}_{1-x}\text{TiO}_{3-y}$. Figure 8 provides the schematic idea of the $x\text{Pb-Pb}_{1-x}\text{TiO}_{3-y}$ material formation.

Specimen heating effect: Consideration of beam heating effect, the energy lost by the electron (when it interacts with the material) in the form of thermal energy results in the increase of temperature. We calculated the beam induced rise in temperature with respect to the time by L.C. Liu *et al.* proposed model³⁶. Figure S11 in the Supplementary Information shows rapid increase in temperature of PTO during initial stage of electron beam irradiation (15.6 K increased at 1 sec); further electron irradiation results in only slight increase in temperature (17.9 K at 200 sec). The result clearly states that the increase of temperature is very low. R. F Egerton *et al.* reported that despite the fact that the high current density involves a very small beam diameter, the temperature rise is usually insignificant (in our case the beam diameter is 50 nm). Therefore the beam induced specimen heating affects less the melting of the PTO nanomaterial. Melting temperature of 30 nm size spherical PbTiO_3 nanoparticle is ≈ 1500 K (bulk melting temperature is 1554 K). The detailed calculation is bestowed in the supplementary information section.

When an e-beam illuminates the precursor, the electron-nucleus interaction leads to the ionization of few atoms in the specimen due to its insulating nature. Consequently, the electric field increases in high level at the edge of the illuminated area due to poor conductivity of the PbTiO_3 nanoparticle. This leads to the ejection of the metallic Pb atom from the precursor. Newly emerged Pb atom grown as Pb nanocrystal, which is formed by nucleation, coalescence and Oswald ripening process. A growth mechanism was proposed to explain the experimental observation and was presented in Fig. S14 (See Supplementary Information). Xing Peng *et al.*²⁶ discovered that the Pb^{2+} cation deficiency is the important candidate as negative thermal expansion materials. Additionally

the Pb nanoparticles are superparamagnetic in nature. In our study, we designed the superparamagnetic nature Pb nanocrystals embedded in cation deficient ferroelectric PbTiO_3 nanoparticle. Blending of these two functional properties in $x\text{Pb-Pb}_{1-x}\text{TiO}_{3-y}$ nanocomposite material leads to open the pathway for new generation multifunctional system. A more detailed study necessitates explaining the electron-perovskite materials interaction and its non-stoichiometric counterpart formation with respect to beam current, thickness of the materials and etc. Nevertheless the fabrication of Pb-NPbTiO₃ ($x\text{Pb-Pb}_{1-x}\text{TiO}_{3-y}$) cation vacant perovskite material via electron beam irradiation in TEM is of great significance for the functional material development and application.

A novel nanocomposite material $x\text{Pb-Pb}_{1-x}\text{TiO}_{3-y}$ is successfully fabricated in simplest technique and it is proven that the proportions in the composite material can be altered by e-beam irradiation. *In situ* HRTEM study on 300 KeV electron beam stimulated pure Pb metal nanoparticles on PbTiO_3 matrix has been investigated. The study reveals that the Pb nucleation and structural fluctuation are controlled by the irradiation time. In addition, the electronic structure and surface features were studied extensively by using the XPS for non-irradiated and irradiated PTO nanomaterials. The novel results reveal that the irradiated PTO exhibits n-type conductor feature, while the non-irradiated PTO exhibits weak p-type. The calculated valence band offset is in good agreement with the reported values. Moreover, the twin and multiple twinned structures are observed in pure Pb metal nanoparticles. The coagulation of Pb-Pb nanoparticle leads to different structures depending on the irradiation time. The sizes of the Pb nanoparticles are various with respect to the internal structure i.e single crystal Pb has a size of 4–6 nm, Twinned Pb has a size of 9–15 nm. The coexistence of this Pb nanocrystal attached to the cation deficient nanoparticle $\text{Pb}_{1-x}\text{TiO}_{3-y}$ perovskite material system is a prominent candidate for functional applications. The study of interaction of PbTiO_3 nanoparticle and electron uncovered that not only the structural transformation occurred in the material and also it is a new approach to fabricate the novel composite system.

Methods

Synthesis of PbTiO_3 nanomaterial. The lead titanate (PbTiO_3) nanoparticles were synthesised by sol-gel method. The precursors used for preparing lead titanate (PT) sol were Lead acetate trihydrate [$\text{Pb}(\text{OCOCH}_3)_2 \cdot 3\text{H}_2\text{O}$], and Titanium IV butoxide [$\text{Ti}(\text{OC}(\text{CH}_3)_2)_4$]. Acetic acid [CH_3COOH] and acetylacetone [$\text{C}_5\text{H}_8\text{O}_2$] utilized as a solvent and a chelating ligand, respectively. All chemicals are purchased from Sinopharm chemical reagent Co.Ltd, China as AR grade. The Pb^{2+} solution is prepared by dissolving Lead acetate trihydrate in acetic acid. The solution is heated and stirred for 25 min. Then 10 ml of equal molar acetylacetone was added into it. Finally, titanium butoxide in stoichiometric ratio is slowly added into the solution with continuous stirring for 25 min to prepare PT sol. The PT sol has dried under in air atmosphere at 120 °C to remove organic residuals. Then, as synthesised powder sample goes through calcinations process. The powder was calcined in small batch (2 g) in silica crucible at 450 °C in air atmosphere for 1 h.

Fabrication of Pb-NPTO nanomaterial. The average size of the nanoparticles is 25 nm (which is used in this study). The PbTiO_3 nanoparticle TEM specimens were prepared by the brief agitation of synthesised material, which is dispersed in ethanol in an ultrasonic bath and dipped over a carbon-film copper grid and placed into the TEM. The sample was allowed to expose in electron beam and study the formation of Pb-NPTO nanomaterial. (Full details of *in situ* HRTEM and XPS study were bestowed in the supplementary Information).

References

- Cohen, R. E. Origin of ferroelectricity in perovskite oxides. *Nature* **358**, 136–139 (1992).
- Nuraje, N. & Su, K. Perovskite ferroelectric materials. *Nanoscale* **5**, 8752 (2013).
- Varghese, J., Whatmore, R. W. & Holmes, J. D. Ferroelectric nanoparticles, wires and tubes: synthesis, characterization and applications. *J. Mater. Chem. C* **1**, 2618 (2013).
- Benidek, N. A., Rondinelli, J. M., Djani, H., Ghosez, P. & Lightfoot, P. Understanding ferroelectricity in layered perovskite: new ideas and insights from theory and experiments. *Dalton Trans.* **44**, 10543 (2015).
- Zhang, X. C. *et al.* Structural, electronic and optical properties of Ilmenite ATiO_3 (A = Fe, Co, Ni). *Mater. Sci. Semicond. Process.* **39**, 6–16 (2015).
- Saha, K. K., Dasgupta, T. S., Mookerjee, A., Saha, S. & Sinha, T. P. Optical properties of perovskite alkaline-earth titanates: a formulation. *J. Phys. Condens. Matter* **14**, 3849–3863 (2002).
- Zhu, X., Liu, Z. & Ming, N. Perovskite oxide synthesis, structural characterization properties and applications. *J. Mater. Chem.* **20**, 4015–4030 (2010).
- Deng, H., Qiu, Y. & Yang, S. General surfactant free synthesis of MTiO_3 (M = Ba, Sr, Pb) perovskite nanostrips. *J. Mater. Chem.* **19**, 976–982 (2009).
- Alammar, T., Hamm, I., Wark, M. & Mudring, A. V. Low-temperature route to metal titanate perovskite nanoparticles for photocatalytic applications. *Appl. Catal. B: Environ* **178**, 20–28 (2015).
- Mao, Y. B., Zhou, H. J. & Wong, S. S. Synthesis, properties and applications of perovskite phase metal oxide nanostructures. *Materials Matters* **5**(2), 50 (2010).
- Maglione, M. *et al.* Defect chemistry in ferroelectric perovskites: long standing issues and recent advances. *Dalton Trans.* **44**, 13411 (2015).
- Ferrarelli, M. C., Tan, C. C. & Sinclair, D. C. Ferroelectric, electrical and structural properties of Dy and Sc co-doped BaTiO_3 . *J. Mater. Chem.* **21**, 6292 (2011).
- Mazzo, T. M. *et al.* Europium-doped calcium titanate: Optical and structural evaluations. *J. Alloys Compd.* **585**, 154–162 (2014).
- Veenhuis, H. *et al.* Light-induced charge-transport properties of photorefractive barium-calcium-titanate crystals doped with rhodium. *Appl. Phys. B* **70**, 797–801 (2000).
- Fadill, F. Z., Lamcharfi, T., Abdi, F. & Aillerie, M. Synthesis and characterization of magnesium doped lead titanate. *Cryst. Res. Technol.* **46**(4), 368–372 (2011).
- Lenin, N. *et al.* Electrical and magnetic behaviour of iron doped nickel titanate ($\text{Fe}^{3+}/\text{NiTiO}_3$) magnetic nanoparticle. *J. Magn. Magn. Mater.* **397**, 281–286 (2016).
- Burnat, D. Synthesis and performance of A-site deficient lanthanum-doped strontium titanate by nanoparticle based spray pyrolysis. *J. Power Sources* **201**, 26–36 (2012).
- Uyi, S. Shu, Y. and Tsugio, S. Solvothermal synthesis and photocatalytic properties of nitrogen doped SrTiO_3 nanoparticles. *J. Nanomaterials* 629727 (2010).

19. Kellati, M. *et al.* Structural and dielectric properties of La-doped lead titanate ceramics. *Mate. Res. Bull* **39**, 867–872 (2004).
20. Gao, F. *et al.* Preparation and electrical properties of yttrium-doped strontium titanate with B-site deficiency. *J. Power Sources* **185**, 26–31 (2008).
21. Park, C. H. & Chadi, D. J. Effect of interstitial hydrogen impurities on ferroelectric polarization in PbTiO₃. *Phys. Rev. Lett.* **84**, 4717–4721.
22. Stashans, A. & Villamagua, L. Schottky defects in cubic lattice of SrTiO₃. *J. Phys. Chem. Solids* **70**, 417–421 (2009).
23. Ganguly, M., Rout, S. K., Woo, W. S., Ahn, C. W. & Kim, I. W. Characterization of A-site deficient samarium doped barium titanate. *Physica B* **411**, 26–34 (2013).
24. Zhao, H. L., Gao, F., Li, X., Zhang, C. J. & Zhao, Y. Q. Electrical properties of Yttrium doped strontium titanate with A-site deficiency as potential anode materials for solid oxide fuel cells. *Solid State Ionics* **180**, 193–197 (2009).
25. Fang, Q. L., Zhang, J. M. & Xu, K. W. Vacancy and doping driven ferromagnetism in BaTiO₃ perovskite. *Physica B* **424**, 79–83 (2013).
26. Peng, X. *et al.* Cation deficiency effect on negative thermal expansion of ferroelectric PbTiO₃. *Inorg. chem. Front* **2**, 1091 (2015).
27. Tanaka, M., Takeguchi, M. & Furuya, K. Behavior of metal nanoparticle in the electron beam. *Micron* **33**, 441–446 (2002).
28. Alymov, M. I., Timofeev, A. A. & Gnedovets, A. G. Coagulation of gold nanoparticle in thin amorphous films under irradiation with a fast electron beam. *Nanotechnologies in Russia* **8**, 727–736 (2013).
29. Gong, J. F. *et al.* In situ synthesis of Ag nanoparticles by electron beam irradiation. *Mater. Charact.* **110**, 1–4 (2015).
30. Guzman, S. S. *et al.* In situ formation of bismuth nanoparticles through electron beam irradiation in a transmission electron microscope. *Nanotechnology* **18**, 335604–10 (2007).
31. Angel, P. D. *et al.* Nucleation and growth of Ni nanoparticles and thin films by TEM electron irradiation. *Catalysis Today* **212**, 194–200 (2013).
32. Ghatak, J., Guan, W. & Mobus, G. In situ TEM observation of lithium nanoparticle growth and morphological cycling. *Nanoscale* **4**, 1754 (2012).
33. Zheng, H., Liu, Y., Mao, S. X., Wang, J. & Huang, J. Y. Beam-assisted large elongation of in situ formed Li₂O nanowires. *Sci. Rep* **2**, 542 (2012).
34. Petford, A. K., Marks, L. D. & Keeffe, M. O. Atomic imaging of oxygen desorption from Tungsten trioxide. *Surface Science* **172**, 496–508 (1986).
35. Liu, Z. Q., Hashimoto, H., Sukedai, E., Song, M., Mitsuishi, K. & Furuya, K. In situ observation of the formation of Fe₃O₄ in Fe₃N (001) due to electron irradiation. *Phys. Rev. Lett* **90**, 255504 (2003).
36. Liu, L. C. & Risbud, S. H. Real time hot stage high voltage transmission electron microscopy precipitation of CdS nanocrystals in glasses: Experiment and theoretical analysis. *J. Appl. Phys.* **76**, 8 (1994).
37. Jencic, I., Bench, M. W. & Robertson, I. M. Electron beam induced crystallization of isolated amorphous regions in Si, Ge, GaP, GaAs. *J. Appl. Phys.* **78**, 2 (1995).
38. Mkhoyan, K. A. & Silcox, J. Electron beam induced damage in wurtzite InN. *Appl. Phys. Lett.* **82**, 859–863 (2003).
39. Huang, W. Q. *et al.* Silicon nanocrystal growth under irradiation of electron beam. *Sci. Rep* **5**, 16682 (2015).
40. Chen, Y. *et al.* Fabrication of nanoscale Ga balls via a Coulomb explosion of microscale silica-covered Ga balls by TEM electron-beam irradiation. *Sci. Rep* **5**, 11313 (2015).
41. Banhart, F. Formation and transformation of carbon nanoparticles under electron irradiation. *Phil. Trans. R. Soc. London. A* **362**, 2205–2222 (2004).
42. Krashenniniv, A. V. & Banhart, F. Engineering of nanostructured carbon materials with electron or ion beams. *Nature Mater* **6**, 723–733 (2007).
43. Kano, J., Kizika, T., Shikanai, F. & Kojima, S. Pure lead nanoparticle with stable metallic surfaces on perovskite lead strontium titanate particle. *Nanotechnology* **20**, 295704–8 (2009).
44. Yamamoto, T., Hirayama, T., Fukunaga, K. & Ikuhara, Y. Electron holographic studies of irradiation damage in BaTiO₃. *Nanotechnology* **15**, 1324–1327 (2004).
45. Meldrum, A., Boatner, L. A. & Ewing, R. C. Electron-irradiation-induced nucleation and growth in amorphous LaPO₄, ScPO₄ and Zircon. *J. Mater. Res.* **12**, 1816–1828 (1997).
46. Pedraza, D. F. Mechanisms of the electron irradiation-induced amorphous transition in intermetallic compounds. *J. Mater. Res.* **1**, 425–442 (1986).
47. Xiao, H. Y., Weber, W. J., Zhang, Y., Zu, X. T. & Li, S. Electronic excitation induced amorphization in titanate pyrochlores: an ab initio molecular dynamics study. *Sci. Rep* **5**, 8265 (2015).
48. Andrievski, R. A. Review of nanostructured materials. *J. Mater. Sci* **38**, 1367–1375 (2003).
49. Hofmeister, H. & Tan, G. L. Shape and internal structure of silver nanoparticles embedded in glass. *J. Mater. Res.* **20**, 1551–1562 (2005).
50. Wu, Y., Takeguchi, M., Chen, Q. & Furuya, K. Defects and their movement in Pb and Ge nanocrystals characterized by ultra high vacuum high resolution transmission microscope. *Appl. Surf. Sci.* **159–160**, 486–491 (2000).
51. Wang, R., Zhang, H. Z., Farle, M. & Kisielowski, C. Structural stability of icosahedral FePt nanoparticles. *Nanoscale* **1**, 276–279 (2009).
52. Pilch, M. & Molak, A. Resistivity switching induced ferroelectric phase of PbTiO₃ studied by XPS and electric conductivity tests. *J. Alloys Compd.* **586**, 488–498 (2014).
53. Gu, H. S. *et al.* Fabrication of lead titanate single crystalline nanowires by hydrothermal method and their characterization. *J. Sol-Gel. Sci. Techn.* **4**, 293–297 (2007).
54. Adamiec, M., Talik, E. & Wojcik, K. Photoelectron spectroscopy of PbTiO₃: Mn single crystal. *J. Alloys Compd.* **442**, 222–224 (2007).
55. Zhu, T. J. & Lu, L. X-ray diffraction and photoelectron spectroscopic studies of (001) oriented Pb(Zr_{0.52}Ti_{0.48})O₃ thin films prepared by laser ablation. *J. Appl. Phys.* **95**, 241–247 (2004).
56. Kozakov, A. T., Kochur, A. G., Polozhentsev, O. E. & Nikolshii, A. V. Electronic structure of single crystal solid solutions Pb_{1-x}Ba_xTiO₃ (0 < x < 1) from X-ray photoelectron spectroscopy and real-space multiple electron scattering calculations. *J. Alloys Compd.* **695**, 3170–3177 (2017).
57. Kurasawa, M. & McIntyre, P. C. Surface passivation and electronic structure characterization of thin films and interfaces. *J. Appl. Phys.* **97**, 104110–9 (2005).
58. Schafrank, R., Li, S., Chen, F., Wu, W. & Klein, A. PbTiO₃/SrTiO₃ interface: Energy band alignment and its relation to the limits of Fermi level variation. *Phys. Rev. B* **84**, 045317–7 (2011).
59. Gonzalez-Martinez, I. G. *et al.* Electron-beam induced synthesis of nanostructures: a review. *Nanoscale* **8**, 11340–11362 (2016).
60. Egerton, R. F., Li, P. & Malac, M. Radiation damage in the TEM and SEM. *Micron* **35**, 399–409 (2004).
61. Egerton, R. F. Outrun radiation damage with electron? *Advanced structural and chemical imaging* **1**, 5 (2013).
62. Banhart, F. Formation and transformation of carbon nanoparticles under electron irradiation. *Phil. Trans. R. Soc. Lond. A* **362**, 2205–2222 (2004).

Acknowledgements

This work is supported by the National Natural Science Foundation of China (No. 51231007, 51571197, 51501194, 51671194, 51521091, and 51401212), National Basic Research Program of China (2014CB921002), and Chinese

Academy of Sciences (QYZDJ-SSW-JSC010). Y. L. T. acknowledges the IMR SYNL-T.S. Kê Research Fellowship and the Youth Innovation Promotion Association CAS (No. 2016177). One of the authors J. S. would like to express the gratitude to Dr. Y. T. Zhou for fruitful discussion. J. S. thanks Mr. Njoku Demian Ifeanyi and Mr. Azim Khan for providing the chemical precursors and timely help. J. S. acknowledges the IMR-CAS Doctoral Fellowship. The authors are grateful to B. Wu of this laboratory for their technical supports on the Titan platform of G2 60-300 kV aberration-corrected scanning transmission electron microscope.

Author Contributions

Y.L.Z. and X.L.M. conceived the project of interfacial characterization in oxides by using transmission electron microscopy; J.S. synthesised the samples; J.S., Y.B.X., L.X.Y., S.L. and Y.L.T. performed the TEM observations. J.S. and Y.J.W. did the XPS data interpretation. All authors participated in discussion and interpretation of the data.

Additional Information

Supplementary information accompanies this paper at doi:[10.1038/s41598-017-09031-5](https://doi.org/10.1038/s41598-017-09031-5)

Competing Interests: The authors declare that they have no competing interests.

Publisher's note: Springer Nature remains neutral with regard to jurisdictional claims in published maps and institutional affiliations.



Open Access This article is licensed under a Creative Commons Attribution 4.0 International License, which permits use, sharing, adaptation, distribution and reproduction in any medium or format, as long as you give appropriate credit to the original author(s) and the source, provide a link to the Creative Commons license, and indicate if changes were made. The images or other third party material in this article are included in the article's Creative Commons license, unless indicated otherwise in a credit line to the material. If material is not included in the article's Creative Commons license and your intended use is not permitted by statutory regulation or exceeds the permitted use, you will need to obtain permission directly from the copyright holder. To view a copy of this license, visit <http://creativecommons.org/licenses/by/4.0/>.

© The Author(s) 2017